

# Surface dynamics of ordered $\text{Cu}_3\text{Au}(001)$ studied by elastic and inelastic helium atom scattering

B. Gans<sup>1,2</sup>, P.A. Knipp<sup>2,3</sup>, D.D. Koleske<sup>1</sup> and S.J. Sibener<sup>1</sup>

*The James Franck Institute, The University of Chicago, 5640 South Ellis Avenue, Chicago, IL 60637, USA*

Received 20 August 1991; accepted for publication 26 September 1991

Inelastic helium atom scattering has been used to measure the surface phonon dispersion curves for the (001) face of the ordered phase of  $\text{Cu}_3\text{Au}$  along the  $\langle 100 \rangle$  (i.e.,  $\bar{\Gamma}-\bar{M}'$ ) direction. We report the spectroscopic observation of two surface phonon modes on this fcc alloy, and present a detailed description of the scattering instrument that was used for making these measurements. The lower-energy surface phonon mode, the Rayleigh wave, has an energy of  $7.1 \pm 0.5$  meV at  $\bar{M}'$ . The higher-lying feature is an optical mode with an energy of  $12.5 \pm 1.0$  meV, which shows little dispersion across the surface Brillouin zone. This phonon mode might be interpreted as a folded Rayleigh mode. The experimentally measured dispersion curves do not agree with those generated by a lattice dynamical slab calculation which uses a pair potential force-field that successfully models the bulk vibrations of the ordered alloy. The best fit to our experimental data indicates that the force constant between the first and second layer Cu atoms needs to be stiffened by  $\sim 20\%$  with respect to the corresponding bulk value.

## 1. Introduction

Understanding the chemical and physical properties of alloy surfaces is important for the further development of heterogeneous catalysts and for the custom design of material interfaces able to withstand corrosive and high-temperature environments. Although a wide variety of clean and adsorbate-covered surfaces have been studied [1], there have been only a few surface studies of intermetallic compounds which comprise ordering binary alloys [2,3].  $\text{A}_3\text{B}$  intermetallic compounds often form fcc lattices of which a simple cubic sublattice consists solely of minority atoms. These are interesting because they exhibit high strength even at elevated temperatures [4]. Samples consisting of both ordered and disordered regions are of further interest, as their physical properties, such as resistance to dislocation prop-

agation and brittleness, can be optimized for a specific application given our present understanding of the relationship between microstructure and micromechanics. For this reason “superalloys” such as  $\text{Ni}_3\text{Al}$  and  $\text{Ti}_3\text{Al}$  are currently used in high-performance applications of the aerospace industry. These alloys exhibit increased hardness in their ordered phase as compared to their disordered phase or their single-metal constituents [4]. In this paper we report detailed surface phonon spectroscopy for the model system  $\text{Cu}_3\text{Au}(001)$ , with the goal being to investigate how interatomic forces differ between the surface and bulk regions of an intermetallic compound.

The  $\text{Cu}_3\text{Au}$  crystal structure and reciprocal space lattice are shown in fig. 1, including the surface Brillouin zones (SBZ) for the ordered and disordered states of the alloy. Low-energy electron diffraction studies (LEED) have established that at low temperatures  $\text{Cu}_3\text{Au}(001)$  exhibits a high degree of long-range order [5–11], with the surface existing as a  $c(2 \times 2)$  structure. Planes perpendicular to the (001) direction consist of alternating layers of either 50% Cu–50%

<sup>1</sup> Also Department of Chemistry.

<sup>2</sup> Present address: Naval Research Laboratory, Washington, DC 20375, USA.

<sup>3</sup> Also Department of Physics.

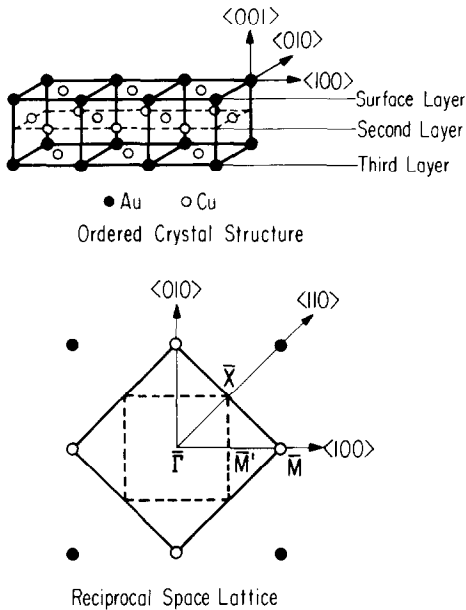


Fig. 1. Top panel: Real space view of the ordered  $\text{Cu}_3\text{Au}$  crystal lattice. Lower panel: Reciprocal space presentation of the surface Brillouin zones for  $\text{Cu}_3\text{Au}(001)$  in its ordered (dashed lines) and disordered (solid lines) states. Open circles in the lower panel denote superlattice points, which disappear above  $T_c$ .

Au or 100% Cu composition. The low-energy ion scattering study (LEIS) of Buck and Wheatley [8] has shown that the (001) surface of the ordered phase terminates exclusively with a layer consisting of 50% Cu–50% Au composition, ordered in a  $c(2 \times 2)$  arrangement.

$\text{Cu}_3\text{Au}$  is particularly interesting because the bulk undergoes a first-order phase transition ( $T_c = 663$  K) to form a substitutionally disordered phase at a temperature well below its melting temperature ( $T_m = 1226$  K) [12–14]. Recent theory [15] and experiments [16] on the (001) surface order–disorder transition indicate that the transition occurs continuously. There is also the possibility that it may also have some first order character at the bulk transition temperature [7]. Although the symmetry is reduced when going from the ordered state to the disordered state, the material maintains an fcc lattice – in contrast to a surface melting transition. Because of this the structural and vibrational properties both above

and below the transition temperature can be investigated in the same way.

We have employed both elastic and inelastic helium atom scattering (HAS) to characterize the structure and vibrational properties of  $\text{Cu}_3\text{Au}(001)$ . HAS is especially well suited for this study since it has extreme sensitivity to the outermost layer of the alloy; i.e., it offers a high degree of “contrast” between the surface and the selvedge region. It is also totally surface nondestructive. The superior energy resolution (0.25–1.0 meV) available with inelastic HAS allows clear identification of low-frequency modes, that may only be separated in energy by a few meV. Such measurements can be viewed as a two-dimensional, surface sensitive, analog to inelastic neutron scattering.

In this paper we will primarily concern ourselves with the dynamical properties of the (001) surface of the ordered system. Future publications will be concerned with the surface structure and phonon spectrum at temperatures near the surface phase transition and above it, when both the surface and the bulk of the alloy become disordered [17]. This paper is organized as follows: We begin with a brief discussion of the kinematics of HAS, along with how it is used as a spectroscopic tool for measuring surface phonon dispersion. Following this section, details of our HAS apparatus will be discussed including the preparation of the  $\text{Cu}_3\text{Au}(001)$  surface. The next section presents our experimental results, including diffraction and inelastic scattering measurements. To interpret the observed phonon modes, lattice dynamics calculations were performed which allowed us to compare the surface force-field with that predicted from the vibrations of the bulk alloy. Our results are then briefly summarized in section 8.

## 2. Kinematics of helium atom scattering

When low-energy helium atoms scatter from a surface, they predominantly scatter elastically into the specular or other diffraction directions. However, some of the incident helium atoms do exchange energy with the surface, through creation

or annihilation of one or more surface or bulk phonons [18]. When cryogenically cooled helium atom beams are used the multiphonon background can be greatly reduced [19], leaving single-phonon exchanges as the primary inelastic channel.

The incident and scattered helium beams are characterized by their incident,  $\mathbf{k}_i$ , and final,  $\mathbf{k}_f$ , wavevectors and by their incident  $E_i = \hbar\mathbf{k}_i^2/2m$  and final  $E_f = \hbar\mathbf{k}_f^2/2m$  energies, where  $m$  is the mass of the helium atom. (Uncapitalized bold letters will designate vectors while capitalized bold letters will designate projections of these vectors onto the surface plane.) The incident and final scattering angles,  $\theta_i$  and  $\theta_f$ , respectively, are defined with respect to the surface normal.  $|\mathbf{K}_i| = |\mathbf{k}_i| \sin \theta_i$  and  $|\mathbf{K}_f| = |\mathbf{k}_f| \sin \theta_f$  are the surface projections of the incident wavevectors.

During the scattering process both surface parallel momentum and total energy are conserved:

$$\mathbf{K}_f = \mathbf{K}_i + (\mathbf{Q} + \mathbf{G}) = \mathbf{K}_i + \Delta\mathbf{K}, \quad (1)$$

$$E_f = E_i \pm \hbar\omega(\mathbf{Q}), \quad (2)$$

where  $\mathbf{G}$  is a reciprocal lattice vector,  $\mathbf{Q}$  is the parallel momentum transfer, and  $\hbar\omega(\mathbf{Q})$  is the energy exchanged to the helium atom by creating (–) or annihilating (+) a single phonon. For in-plane scattering, the observable modes must have some shear vertical (SV) character.

When the scattering conditions ( $\theta_i$ ,  $\theta_f$ ,  $E_i$ ) are established and the equations for conservation of surface parallel momentum (1) and the total energy (2) are combined, a useful relationship develops between the phonon energy as a function of the parallel momentum transfer. This relationship:

$$\omega(\mathbf{Q}) = \frac{\hbar\mathbf{k}_i^2}{2m} \left( \frac{\sin \theta_i - (\Delta K/k_i)}{\sin \theta_f} \right)^2 - \frac{\hbar\mathbf{k}_i^2}{2m}, \quad (3)$$

is called a “scan curve”, and represents the locus of energy versus momentum transfer that is observable for a given set of scattering conditions. Such scan curves are useful when assigning peaks in a time-of-flight spectrum, and are shown with our inelastic scattering results. In previous helium scattering experiments by other groups the angle between the incident beam and the detector,

$\theta_i + \theta_f = \theta_{\text{BD}}$ , has been typically fixed (usually at  $\theta_{\text{BD}} = 90^\circ$ ) and the crystal was rotated to obtain the needed momentum transfer. However, in our machine  $\theta_{\text{BD}}$  is variable, which accounts for the  $\sin \theta_f$  term in the denominator. A detector which can be rotated independently while keeping the incident conditions fixed is useful for the analysis and interpretation of elastic and inelastic data. This is especially true when quantum scattering calculations are performed, because a single calculation for a given  $\mathbf{k}_i$  yields results for all final scattering angles.

### 3. Apparatus

#### 3.1. Overview

Experiments were performed in a high-resolution helium scattering apparatus which is schematically shown in fig. 2 [20]. The machine consists of a helium nozzle beam source, an ultrahigh vacuum scattering chamber, and a rotatable, triply-differentially pumped quadrupole mass spectrometer. The essential requirements for the study of surface structure and surface phonon spectroscopy by helium atom scattering require that there be (1) good energy and wavevector resolution, (2) good detector sensitivity with low mass 4 background, and (3) high beam intensity. A supersonic nozzle beam source meets the requirements of energy resolution and beam intensity. The detector, which has several stages of differential pumping provides sufficiently low mass 4 background during scattering ( $\sim 10^{-14}$  mbar He partial pressure) to permit the detection of low cross-section scattering events. The detector rotates  $\pm 20^\circ$  about the crystal normal in the scattering plane. The important features of the machine design and performance are summarized in table 1. In the present configuration the total flight path (chopper–ionizer) is 110 cm, and the crystal–ionizer distance is 55 cm.

#### 3.2. Beam source

The nozzle–skimmer region is pumped by a 10000  $\ell/s$  diffusion pump which has its foreline

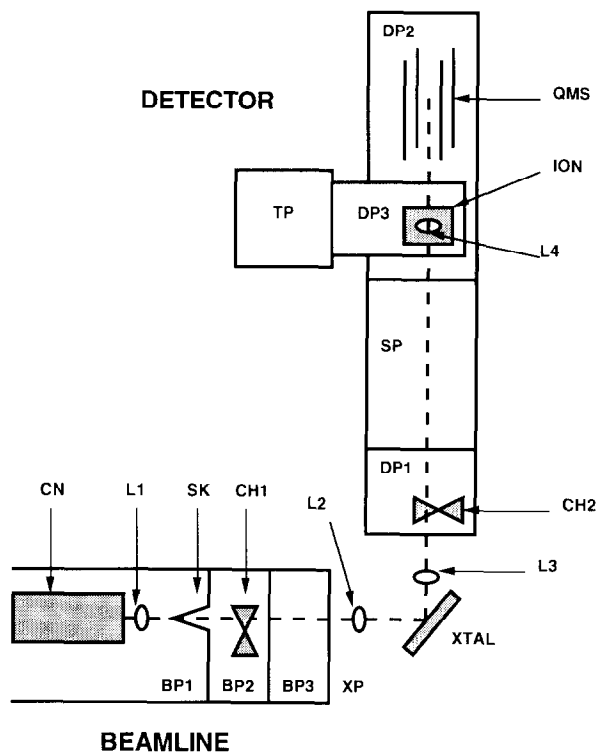


Fig. 2. Schematic view of the helium scattering apparatus, showing the beam source, crystal chamber, and rotatable detector. Abbreviations: CN: cryogenic nozzle, L1–4: laser interaction volumes, SK: skimmer, BP1–3: beamline pumping regions, CH1: pre-collision chopper, XP: crystal pumping region, CH2: post-collision chopper, DP1–3: detector pumping regions, SP: spacer section, TP: turbomolecular pump, ION: electron bombardment ionizer, QMS: quadrupole mass spectrometer.

backed by a Roots blower. Typical throughput of the source region is  $\sim 10$  Torr  $\ell/s$ . The expansion is subsequently skimmed by an electroformed conical skimmer, chopped by a mechanical chopper, and then collimated by two apertures to  $0.31^\circ$  before it enters the bell jar where it forms a 3.7 mm diameter spot on the target crystal (when at normal incidence). The second differential region contains a mechanical chopper (14.986 cm diam) mounted on a linear motion feedthrough that allows one of five different modulation patterns to cross the beam axis. For time-of-flight measurements we typically used a pattern containing four 0.0508 cm wide slits, yielding a duty cycle of  $\sim 1\%$ . This arrangement

transmits a particle pulse of 10  $\mu\text{s}$  FWHM when the chopper wheel is spun at 150 Hz. The chopper region is pumped by an 800  $\ell/s$  diffusion pump. The third differential pumping stage is a buffer to the scattering chamber and is pumped by a 160  $\ell/s$  diffusion pump. The nozzle of the beam source is attached to the second stage of a closed cycle helium refrigerator which can cool the nozzle down to 40 K. The temperature of the nozzle region (and therefore the energy of the beam) is both monitored and regulated by a Lakeview Cryotronics DRC-81C temperature controller. Typically, intermediate nozzle temperatures (80–130 K) were used by both heating and cooling the nozzle. A temperature stability of  $\pm 0.2$  K was achieved with this arrangement. To ensure minimal thermal losses due to radiative heating the nozzle region was constructed out of OFHC copper and wrapped with Mylar superinsulation. To minimize the thermal load on the second stage of the refrigerator the gas was also precooled to 80 K using the first stage of the

Table 1  
Some important parameters of the He-atom surface scattering apparatus

Beam source	
Nozzle stagnation temperature (K)	70–150 (100–150) <sup>a)</sup>
Nozzle diameter ( $\mu\text{m}$ )	$25 \pm 5$ ( $12.5 \pm 2.5$ ) <sup>a)</sup>
Nozzle stagnation pressure (psi)	400–800 (1500–2000) <sup>a)</sup>
Chopper–target distance (cm)	54.9
Chopper wheel frequency (Hz)	150–175
Chopper slit width (in.)	0.02
Repetition rate (Hz)	600–700
Chopper pulse width ( $\mu\text{s}$ )	10 (FWHM)
Relative velocity spread ( $\Delta v/v$ )	$\sim 1$ –1.5%
Total beam divergence (deg)	0.31
Beam spot size on crystal (cm)	0.36
Chopper–detector distance (cm)	110
Target–ionizer distance (cm)	55
Ionizer length (cm)	$\sim 1$
Ionizer aperture diam (cm)	0.635
He part. press. in ionizer (mbar)	$10^{-14}$
Detector angular acceptance (deg)	
when viewed from the crystal	0.67
when viewed from the source	0.33

<sup>a)</sup> These values are for a beam made with a 12.5  $\mu\text{m}$  nozzle.

expander. Nozzle apertures could be easily changed by replacing the electron microscope aperture which served as the actual expansion nozzle. The beam flux produced with this triply pumped beamline for a typical 80 K and 25  $\mu\text{m}$  nozzle, as quantified by a modified ionization gauge, was  $6.0 \times 10^{19}$  atoms/(srs). The velocity spread of the beam was  $\sim 1\%$ .

### 3.3. Scattering chamber

The scattering chamber contains standard surface analysis equipment, i.e., a sputter ion gun, glancing incidence electron gun, X-ray source and a double-pass cylindrical mirror analyzer for Auger and X-ray photoelectron spectroscopy (XPS), in addition to a reverse view LEED that provides a quick and easy assessment of surface order and crystallographic orientation. The sample manipulator is offset 5 cm from the bell jar center and is mounted on a doubly differentially pumped rotatable lid which is sealed by three spring-loaded teflon gaskets. This mounting arrangement enables the crystal to be moved to several surface analysis positions (Auger, XPS, or LEED) or to the scattering center while maintaining the ability to azimuthally rotate the crystal. The scattering chamber is pumped by a 2400  $\ell/\text{s}$  diffusion pump and a 60  $\ell/\text{s}$  DI ion pump. This pumping arrangement, in conjunction with the cryogenic pumping provided by the crystal mount (see below) sustains a pressure of  $1\text{--}2 \times 10^{-9}$  Torr when the beam is on and produces a base pressure in the high  $10^{-11}$  Torr range when the beam is off.

The crystal sample was attached to a manipulator that could translate the crystal in three orthogonal directions, provide tilt, and rotate the crystal  $180^\circ$  in polar angle and  $90^\circ$  in its azimuth. The  $\text{Cu}_3\text{Au}(001)$  sample was mounted on a standard 20 W Mo button heater (Spectra-Mat, E292) that could heat the sample to above 700 K. A chromel–alumel thermocouple was attached to the crystal for monitoring its temperature. The crystal mount was cooled by an OFHC copper braid connected to a closed cycle helium refrigerator.

### 3.4. Detector

The rotating detector consists of three precision-machined concentric chambers that are mounted on an optical rail support system which provides relatively easy insertion and autoalignment of its individual sections. The detector assembly rests on a large square steel channel, mounted onto a turntable with precision bearings. Its angular position is read to a precision of  $0.01^\circ$  by an optical encoder which is directly mounted on the turntable that supports the entire detector. It is coupled to the UHV chamber by a flexible stainless steel bellow. The angular acceptance of the detector was set for these experiments at  $0.67^\circ$  when viewed from the crystal ( $0.30^\circ$  when viewed from the nozzle source). The detector itself is an Extrel quadrupole mass spectrometer equipped with an axial electron bombardment ionizer and an off-axis channeltron, an arrangement that allows a clear line-of-sight along the entire detector that is especially useful when aligning the detector to the rotation axis and scattering center. The first differential chamber contains the first defining aperture and provides space for a post-collision chopper. The next chamber houses a detachable spacer tube which is 44.22 cm in length and allows a choice between two different nominal flight-path lengths: 55 or 100 cm. The spacer can be easily removed without perturbing the alignment or changing the number of differential pumping regions in the detector because the whole detector is mounted on optical rails. The spacer tube was removed in this experiment. The last chamber houses the ionizer and quadrupole rods. The first and last differential regions of the detector are diffusion pumped, liquid nitrogen trapped and interlocked to electro-pneumatic valves. The ionizer region is independently pumped by a 170  $\ell/\text{s}$  turbopump (Balzers) which is backed by a 63  $\ell/\text{s}$  diffusion pump. This pumping scheme provides the high compression ratios that are needed for evacuating light gases with virtually no backstreaming. Also, the ionizer chamber is separately pumped from the following quadrupole rod region, thus eliminating multiple (echo) trajectories in the

vicinity of the ionization volume and further reducing the mass 4 background.

### 3.5. Data collection

Timing and data collection was computer controlled by a Digital LSI 11/73 minicomputer that was interfaced to a CAMAC dataway. The mass spectrometer pulses were amplified and discriminated before being sent to a home-built multi-channel scaler that has a minimum dwell time of  $0.25 \mu\text{s}$ . A dwell time of  $3 \mu\text{s}/\text{channel}$  was typically used for the time-of-flight data reported in this paper. For the diffraction scans a gated CAMAC 24-bit (125 MHz) scaler was used to collect the data. An optical encoder interfaced to the computer kept accurate track ( $0.01^\circ$ ) of the detector position throughout all diffraction and time-of-flight scans.

## 4. Crystal preparation

The  $\text{Cu}_3\text{Au}(001)$  crystal was the same as used by Graham [9], and was previously aligned and polished. No further polishing was attempted in order to avoid preferentially removing Cu from the surface [10]. During the previous experiments the crystal's bulk had been depleted of its major impurities. The surface was cleaned by  $0.5 \text{ keV Ar}^+$  ion bombardment with the crystal held at room temperature. The main contaminant was carbon, although occasionally oxygen was also present. Cycles of  $\text{Ar}^+$  ion bombardment of  $\sim 30$  min duration were repeated until the surface was determined to be clean by Auger spectroscopy ( $< 0.05\%$  carbon contamination). The  $60 \text{ eV Cu}$  and  $70 \text{ eV Au}$  Auger peaks [7] were used to monitor the surface composition [6,7]. Since the strengths of these transitions are approximately equal and do not overlap, the relative peak heights are directly proportional to the atomic composition [7].

After the surface was clean the temperature was increased to  $630\text{--}660 \text{ K}$  for a few minutes and annealed for  $15\text{--}18 \text{ h}$ . The temperature slowly dropped during annealing to  $590\text{--}610 \text{ K}$ . After the first few crystal preparations we did not go

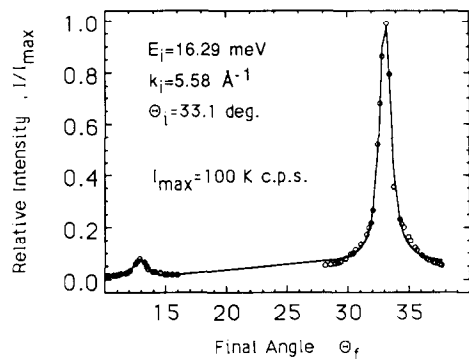


Fig. 3. Diffraction scan along the  $\langle 100 \rangle$  ( $\bar{\Gamma}-\bar{M}'$ ) direction. The open circles are the diffraction data and the solid line is a simulation of the diffraction scan taking into consideration the instrument function.

above the bulk first-order transition temperature,  $T_c = 664 \text{ K}$ . This was possible because the surface begins to disorder  $10\text{--}60 \text{ K}$  below  $T_c$  [5,7,11], which implies that there is sufficient mobility to anneal and hence order the surface at temperatures just below  $T_c$ . After annealing the crystal was cooled at a rate of  $7 \text{ K}/\text{min}$  to an intermediate temperature ( $\sim 470 \text{ K}$ ) and held there for  $1\text{--}2 \text{ h}$  before scattering. During this time the surface composition and order were checked by Auger spectroscopy and LEED. The Auger spectrum for a well annealed sample, i.e., one having  $50\% \text{ Cu}\text{--}50\% \text{ Au}$  composition, produced a  $\text{Cu}_{60}/(\text{Cu}_{60} + \text{Au}_{70})$  Auger peak-to-peak height ratio of  $0.52 \pm 0.02$ , in excellent agreement with literature values [10].

Fig. 3 shows a diffraction scan taken from a clean and well ordered room temperature surface along the  $\bar{\Gamma}-\bar{M}'$  direction. Typical HAS and LEED diffraction profiles had well defined superlattice (half-order) spots with low diffuse background. Occasionally closer examination of the diffraction profiles revealed sharp doublets of both the integral and superlattice diffraction rods aligned along the  $\langle 110 \rangle$  direction. (McRae and Malic [7] have previously reported such faceting along the  $\langle 110 \rangle$  direction with a facet tilt angle of  $\sim 1^\circ$ .) As the surface was heated (fig. 4), the superlattice peak intensity due to the  $c(2 \times 2)$  ordered surface slowly decreased and totally disappeared at  $660 \text{ K}$ . (A high-resolution HAS in-

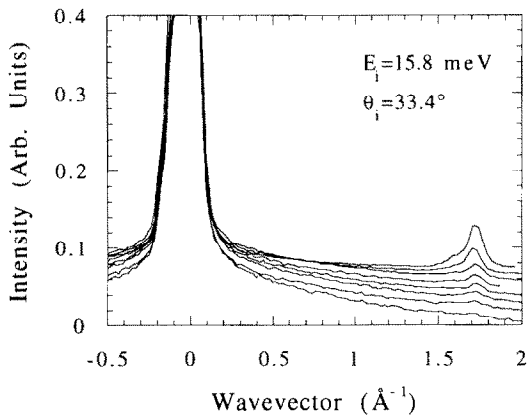


Fig. 4. Angular profiles of the superlattice peak versus crystal temperature. The diffraction scans are presented, from top to bottom, for  $T = 311, 500, 573, 601, 625, 638, 646$  and  $673$  K.

vestigation of the temperature dependence of the superlattice peak intensity will be reported elsewhere [17].) The superlattice peak intensity was usually between 5 and 10% of the specular intensity for the range of scattering conditions used here, and occurred at  $G = 1.67 \pm 0.1 \text{ \AA}^{-1}$ , in agreement with the bulk lattice constant [21]. The solid line in fig. 3 is a fit to the diffraction data taking into consideration the instrument function

of the machine. The transfer width of the machine under these scattering conditions was  $115 \text{ \AA}$  [22]. Comparing the width of the diffraction profile to the computed instrument function, the average domain size of the ordered regions on the surface was found to be approximately  $70 \text{ \AA}$ .

## 5. Results

After a clean and well ordered surface was prepared, inelastic helium scattering was used to map out the surface phonon dispersion curves along the  $\bar{\Gamma}-\bar{M}'$  symmetry direction. The data points were extracted from a series of TOF spectra, taken with different beam energies, incident angles, and final angles. For all TOF spectra shown here the temperature of the crystal was held at  $300$  K.

A series of TOF spectra taken with a fixed incident beam energy,  $E_i = 16.0$  meV, and a fixed incident beam angle,  $\theta_i = 36.4^\circ$ , are shown in fig. 5a. Below these TOF spectra are shown the corresponding time-of-flight profiles transformed into energy spectra, fig. 5b. The corresponding scan curves for these TOF spectra are shown in

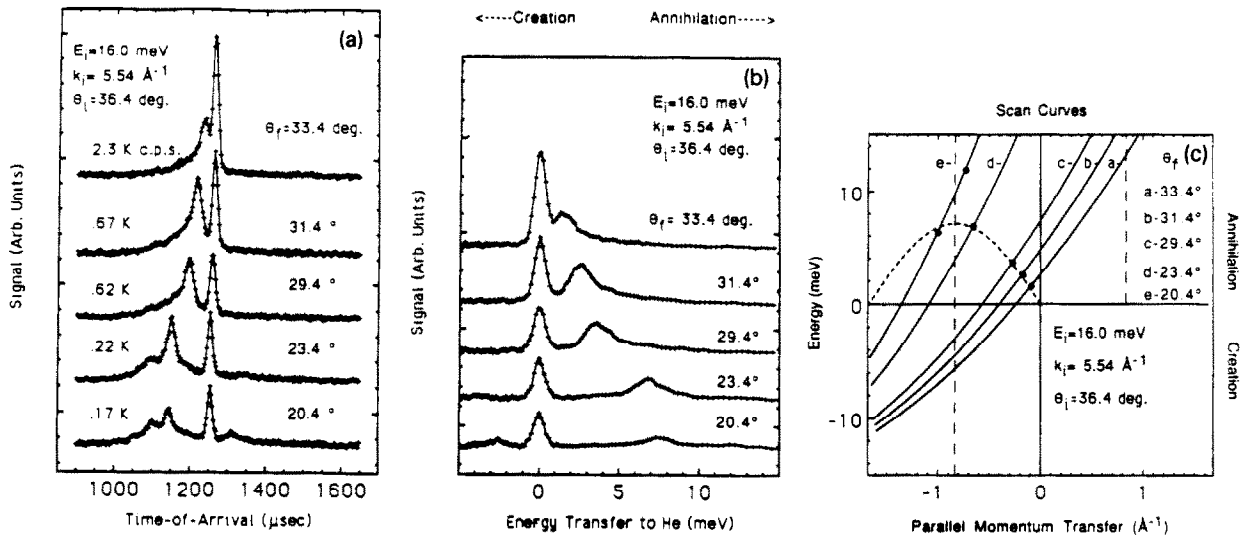


Fig. 5. Inelastic HAS data taken on the  $\text{Cu}_3\text{Au}(001)$  surface. (a) A series of time-of-flight (TOF) spectra taken with fixed incident kinematics. The elastic flight time occurs at  $1254 \mu\text{s}$  for these spectra. The (+)'s are the experimental data and the solid lines are fits to the data. (b) Energy transformed TOF data from (a). (c) The solid lines are scan curves (eq. (3) from text) for the initial and final scattering conditions:  $\theta_i = 36.4^\circ$ ,  $E_i = 16.0$  meV, and  $\theta_f = 33.4^\circ, 31.4^\circ, 29.4^\circ, 23.4^\circ$  and  $20.4^\circ$ . The dashed line is representative of the Rayleigh wave dispersion, and is a sinusoid scaled in energy to  $7.1$  meV. For a discussion of the spectral features see text.

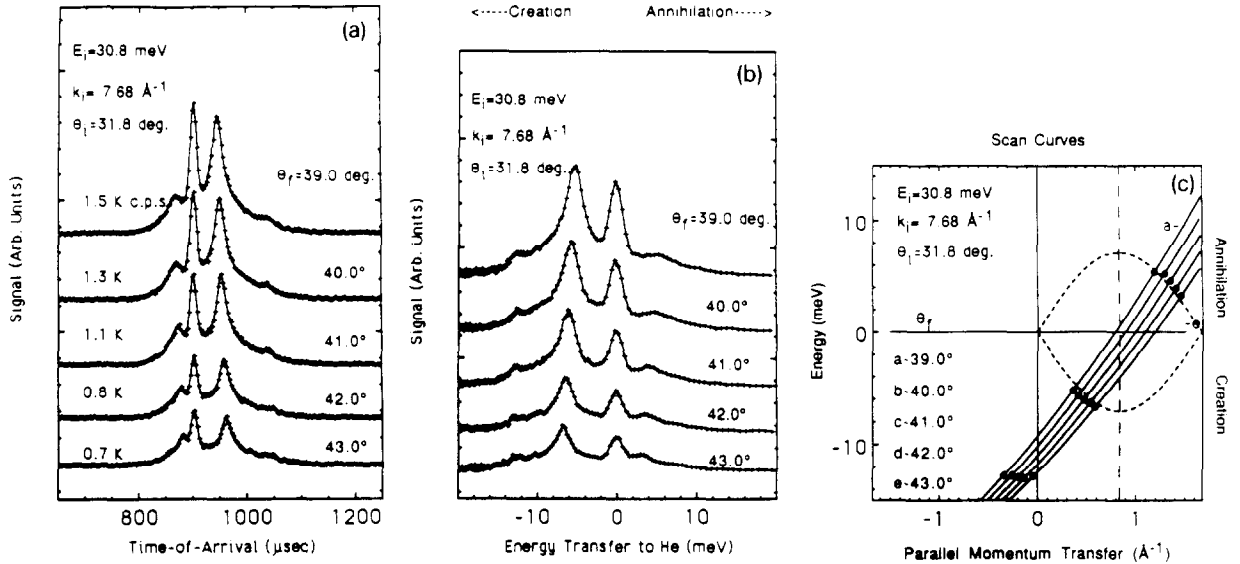


Fig. 6. Same as fig. 5, except for the following incident and final conditions:  $\theta_i = 31.8^\circ$ ,  $E_i = 30.8$  meV, and  $\theta_f = 39.0^\circ$ ,  $40.0^\circ$ ,  $41.0^\circ$ ,  $42.0^\circ$  and  $43.0^\circ$ . The elastic flight time occurs at  $902 \mu\text{s}$  for these spectra. For a discussion of the spectral features see text.

fig. 5c. The intersections of the scan curves with the surface phonon dispersion curves yield peaks in the TOF spectra whose energy loss (gain) features correspond to the creation (annihilation) of single surface phonons.

The most intense feature in each TOF spectrum is the diffuse elastic peak, which appears at the specular time of arrival and corresponds to zero energy transfer. These diffuse elastic peaks can be attributed to static surface disorder [23]. The second most intense feature is an energy gain peak due to the annihilation of a single Rayleigh phonon. As the detector angle moves further away from the specular angle towards the zone edge, the Rayleigh peak disperses and the temporal separation of this peak from the elastic peak increases. Each of the TOF spectra were fit to extract the correct positions of the inelastic features. These peak channels in the TOF spectra were then transformed to find the corresponding energy and momentum of the surface phonon.

A similar set of plots (scan curves, TOF profiles, energy spectra), with  $E_i = 30.8$  meV and  $\theta_i = 31.8^\circ$ , are shown in fig. 6. These TOF spectra show, in addition to the diffuse elastic and single Rayleigh phonon loss and gain peaks, higher en-

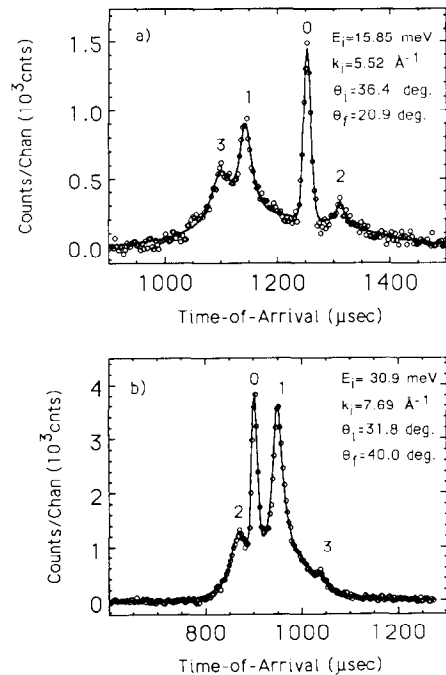


Fig. 7. Two TOF spectra which sample the optical mode at  $\bar{M}$  (a), and at  $\bar{\Gamma}$  (b). The open circles are the experimental data and the solid line is a fit to the data. The peak labels correspond to: (0) diffuse elastic scattering, (1,2) Rayleigh wave, and (3) optical mode.

ergy losses due to the interaction of the helium atom with an “optical mode”. This mode is more clearly shown on an expanded scale in fig. 7, which shows spectra taken with two different beam energies that sample the optical mode at  $\bar{M}'$  (panel a) and  $\bar{\Gamma}$  (panel b). The solid lines plotted in fig. 7 are fits to the TOF data. The four peaks in fig. 7 which result from the fit are labelled as follows: the diffuse elastic peak (0), the most intense Rayleigh peak (1), a less intense Rayleigh peak (2), and the optical mode (3). Also included in these fits is a broad Gaussian peak, intended to approximate both the multiphonon and bulk phonon scattering. In most spectra the diffuse intensity is larger than any inelastic feature, and the intensity of the optical mode is much less than the intensity of the Rayleigh mode. This difference in intensity between the Rayleigh wave and optical mode is due, in part, to the fact that the inelastic scattering intensity varies as  $1/\{\omega[1 - \exp(-h\omega/kT)]\}$  [24], which for  $h\omega \ll kT$  varies as  $1/\omega^2$ . The difference in intensity may also be due to the size difference between the larger Au and the smaller Cu atoms on the surface. It will later be shown that the Rayleigh wave excitation at the Brillouin zone edge largely involves displacements of the Au, while the optical mode involves displacements of the Cu. When

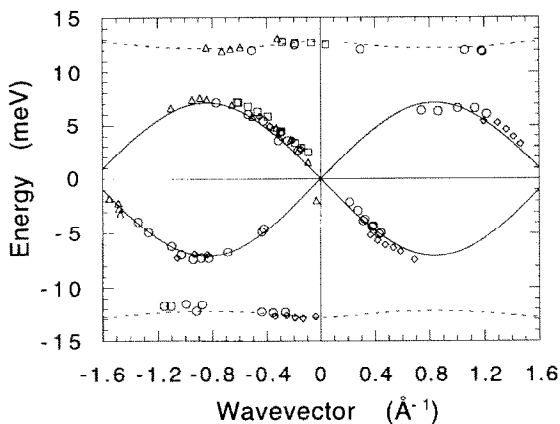


Fig. 8. All data accumulated along the  $\bar{\Gamma}-\bar{M}'$  direction, presented in the extended surface Brillouin zone. Solid lines and dashed lines come from the calculations shown in fig. 10b, and represent the Rayleigh wave and optical mode, respectively. All data were taken with a room temperature crystal.

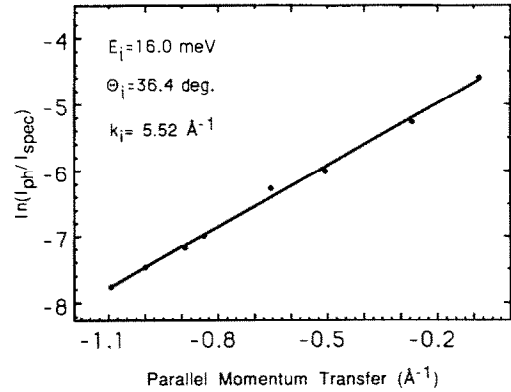


Fig. 9. Logarithmic plot of the decay of Rayleigh wave intensity with increasing parallel momentum transfer. The slope of the straight line drawn through the data corresponds to  $I/I_{\text{spec}} = C \cdot \exp[-Q/(0.32 \text{ \AA}^{-1})]$ .

the collision time becomes long relative to the mean vibrational period of the mode, the induced forces of the mode on the helium atom trajectory cancel, which reduces the inelastic scattering cross section [25]. These reasons may help to explain why the optical mode intensity is reduced as compared to the Rayleigh intensity.

An extended zone plot which summarizes our inelastic scattering data is shown in fig. 8. These data were taken using a variety of incident and final conditions. The energy of the Rayleigh mode at  $\bar{M}'$  is  $7.1 \pm 0.5$  meV, and the upper mode is  $12.5 \pm 1.0$  meV.

We conclude this section by noting that scattering from phonons with large values of parallel momentum transfer,  $Q_{\parallel}$ , are reduced by the “Armand effect” which takes into account the finite size of the helium atom and its simultaneous interaction with several surface atoms [26]. This effect, which is most relevant to smooth metal surfaces, is seen in fig. 9 as an approximately exponential drop-off of intensity, similar to the theoretical and experimental results of ref. [26] at high  $Q$ . This behavior is quantitatively related to the value of the (spatial) turning point of the helium–surface interaction potential. A survey of this behavior on different metal surfaces may provide better insight into how the scattering helium atom couples with the surface.

## 6. Surface force field analysis

A good starting point for a dynamical analysis of surface vibrations is first to construct a force constant model which adequately models the bulk vibrations, as measured by inelastic neutron scattering. An analysis of the bulk neutron scattering data of Katano et al. reveals that the bulk vibrations can be well fit by an extensive 24-parameter force constant model which uses first- through fourth-neighbor interactions, including angle-bending interactions [27]. However, the proper way to modify such a complicated model to describe the surface region is unclear.

To simplify the physical picture of the bulk vibrations and to reduce the number of potential parameters that might need to be modified to match to the surface spectrum, we have modelled the bulk vibrations using pair potentials. This approach easily allows the estimation of the effects of cleavage on the statics and dynamics of a free surface [28]. Noncentral interactions such as angle-bending terms have not been used. A similar pair potential model has recently been used to model the surface modes on  $\text{NiAl}(110)$  [29].

Implementation of the model consists of fitting the first- and second-nearest-neighbor atom interactions to two-body potentials. Each two-body potential consists of a quadratic part [ $=\phi_j'' \times (|\mathbf{r}| - |\mathbf{r}_0|)^2$ ], which is essentially the radial force constant, and a linear part [ $=\phi_j' \times (|\mathbf{r}| - |\mathbf{r}_0|)$ ], which is a tension (or “tangential force constant”) between the atoms. For  $\text{Cu}_3\text{Au}$  there are four possible pair interactions between the first- and second-nearest neighbors (which are listed in table 2), thereby requiring a total of eight fitting

parameters. To ensure crystal stability with respect to changes in the overall atomic density, it is necessary that an appropriately weighted sum of the four tensions vanishes. A fit to the bulk vibrational data was performed to find the values of eight parameters, less the tension constraint. This fit to the bulk data gave a value of  $\chi_{\text{red}}^2 = 7.2$ , and the values are shown in table 2.

To calculate the surface phonon dispersion, a lattice dynamics calculation was performed using the slab technique [30]. The slab consists of eight double-layers, each consisting of one layer of Cu and one layer of 50% Cu–50% Au. The total slab is 16 atomic layers (30 Å) thick and is attached to a rigid substrate. This leaves one free surface, unlike the slabs used in ref. [30]. Due to reflection symmetry along the  $\bar{\Gamma}$ – $\bar{M}'$  direction, the sagittal [shear vertical (SV) and longitudinal] modes are decoupled from the shear horizontal (SH) modes. The later are invisible to in-plane He scattering so do not concern us here. This reduces the size of the Hermitean matrix that needs to be diagonalized from  $96 \times 96$  to  $64 \times 64$ . The matrix diagonalization yields the correct frequency, amplitude, and polarization for all modes except for those at small wavevector and low frequency. These modes at large wavelength and low frequency can, however, be deduced from elastic theory [31], and in this limit the Rayleigh wave has a velocity of 1760 m/s along the  $\bar{\Gamma}$ – $\bar{M}'$  direction.

When a slab calculation is carried out using the unmodified bulk values two modes with large shear vertical component are found which are localized to the surface. These correspond to the two experimentally observed modes. This calcula-

Table 2  
 $\text{Cu}_3\text{Au}(001)$  force constants

$j$	Atom 1– atom 2	1st/2nd neighbor	Bulk fit (N/m)		Surface fit (N/m)	
			$\phi_{jb}'$	$\phi_{jb}''$	$\phi_{js}'$	$\phi_{js}''$
1	Au–Cu	1st	40.4	1.5	40.4	0.8 <sup>a)</sup>
2	Cu–Cu	1st	11.1	–1.0	13.3 <sup>b)</sup>	–0.3 <sup>a)</sup>
3	Au–Au	2nd	–5.1	–4.6	–5.1	–4.6
4	Cu–Cu	2nd	4.1	1.1	4.1	1.1

<sup>a)</sup> Indicates modified surface tension terms used in fig. 10a.

<sup>b)</sup> Indicates modified surface force constant term used in fig. 10b.

tion was performed within the partial harmonic approximation, which means that the surface atoms sit at their bulk terminated values. However, this surface geometry is artificial in that the atomic positions are not at their equilibrium values. When allowed to relax by a procedure outlined by Feuchtwang [28] the surface atoms tend to move out of the surface plane due to the nonvanishing first-derivative terms of the potential. This relaxation results in a rumpled surface where the Au positions remain approximately unchanged but the Cu atoms are displaced outwards from the surface by 0.2 Å. These results contradict previous LEED and ion scattering experiments, which suggested that the first-layer Au atoms are displaced outwards from the surface by 0.1 Å, while the Cu positions are unchanged [32,33].

To compensate for this geometric discrepancy, we altered the tensions in the vicinity of the surface. Specifically, the magnitudes of the tensions  $\phi'_{js}$  of both (i.e., Au–Cu and Cu–Cu) first-nearest-neighbor atom pairs were reduced from those of their bulk counterparts  $\phi'_{jb}$ , as shown in table 2. This brings the theoretical prediction into agreement with the experimentally observed surface rumpling while ensuring crystal stability with respect to changes in the overall atomic density.

Using these surface tensions  $\phi'_{js}$  and the bulk force constants  $\phi''_{jb}$ , the phonon dispersion was calculated and is shown in fig. 10a. Note that the upper mode is degenerate with the bulk band, so is in fact a surface “resonance”. The calculated values for the Rayleigh wave agree well with the experimental data; however, the upper mode is too low in energy. To fit the higher energy optic mode a 20% stiffening of first-nearest-neighbor Cu–Cu force constant  $\phi''_{2b}$  is needed. The results of this slab calculation are shown in fig. 10b. This is approximately the same amount of stiffening needed to match the EELS experimental data for the Rayleigh wave on Cu(001) [34].

The stiffening of  $\phi''_{2b}$  affects the optical mode strongly, while it leaves the Rayleigh wave virtually unchanged. The choice to stiffen this force constant over others can be understood by considering the phonon mode displacements for these two modes. The phonon mode displacements are

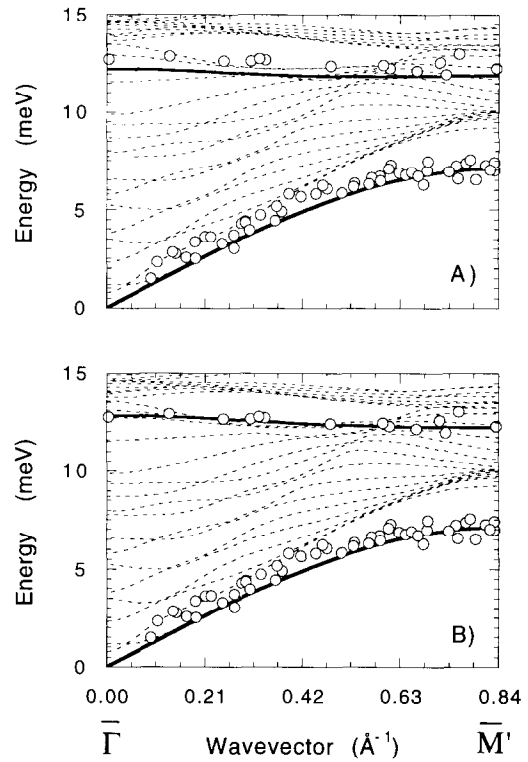


Fig. 10. Slab calculations as outlined in the text. (a) Model using  $\phi'_{js}$  and the unmodified  $\phi''_{jb}$ , which are listed in table 2. (b) Same as (a) except  $\phi''_{2s}$  has been stiffened by 20%. The open circles are the data folded onto the first surface Brillouin zone. The dashed lines represent the continuum of the bulk modes.

shown in fig. 11 for the optical and Rayleigh modes at  $\mathbf{Q} = \bar{\mathbf{M}}'$  and for the optical mode at  $\mathbf{Q} = \bar{\Gamma}$ . Near  $\mathbf{Q} = \bar{\mathbf{M}}'$ , the Rayleigh wave displacement vectors involve predominantly SV motion of the first-layer Au atoms. At low wavevector the Rayleigh wave penetrates deeply into the bulk, so is insensitive to surface details. The optical mode consists primarily of out-of-plane motion of the first-layer Cu atoms, throughout the SBZ, essentially due to the Cu:Au mass ratio. Hence the optical mode is more sensitive to changes in those force constants which connect the first- and second-layer Cu atoms.

Although this model fits our data quite well, it is by no means unique. For example, another model was created in which the first-nearest-neighbor tensions  $\phi'_{1s}$  and  $\phi'_{2s}$  were held at their

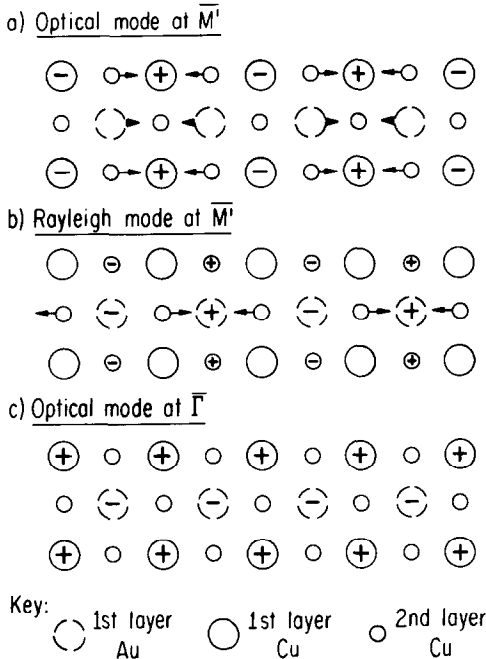


Fig. 11. Top view of the polarizations of the vibrational modes for the Rayleigh mode at  $\bar{M}'$ , and the optical mode at  $\bar{\Gamma}$  and  $\bar{M}'$ . As stated in section 5, the predominant displacements of the atoms in panels (a) through (c) occur in the topmost layer and are, respectively: SV Cu, SV Au, and SV Cu.

bulk values while the values of next-nearest-neighbor tensions were modified,  $\phi'_{3s} = 1.5\phi'_{3b}$  and  $\phi'_{4s} = 3.2\phi'_{4b}$ . This result gave the correct geometry at the surface but predicted a shift by  $0.3 \text{ \AA}$  of the third-layer Cu atoms toward the surface (and hence consistent with the results of refs. [32,33]). Within this latter model a stiffening of  $\phi''_{2b}$  by 45% is needed to match our experimental data. A common feature of all models we explored was that the force constant between first- and second-layer Cu atoms required significant stiffening. Electronic structure calculations that yield surface phonon dispersion curves would be most useful at this time.

## 7. Discussion

The justification for stiffening  $\phi''_{2b}$  depends on bonding changes which occur at the surface. In the bulk of noble metals, two forces oppose each

other, one which is a pairwise repulsion between the atoms due to filled d shells, and the second is a multi-atom attraction which is a consequence of the sp electrons and the sp-d hybridization [35]. These two forces comprise the ansatz for the development of the “embedded atom method” [36]. At the surface, the d shells remain full, which gives rise to an expansive pressure, and the sp electrons tend to lower their energy by flowing into the attractive mantle between the first and second layers, enhancing interplanar bonding. This enhancement in interlayer electron density manifests itself on noble metals in a reduced first and second interlayer spacing [37], and simultaneous stiffening of  $\phi''_{2b}$ .

As the alloy disorders, subtle binding differences have been observed in the electronic structure. The major consensus from these experiments [38,39] and theory [35,40] is that  $\text{Cu}_3\text{Au}$  is a “common d-band alloy” where the Au bands are concentrated at the bottom of the d band and the Cu bands are concentrated at the top of the d band [38]. As the bulk disorders the most predominant effect observed in the spectra is a broadening in the Au bands [38]. Similar broadening is also observed in the UV photoelectron spectra measured on  $\text{Cu}_3\text{Au}(001)$  above and below the transition temperature and appears to occur continuously [39]. Recent measurements by X-ray absorption near edge structure (XANES) and XPS show that the Au 5d count is depleted upon formation of  $\text{Cu}_3\text{Au}$ , and that the ordered  $\text{Cu}_3\text{Au}$  is more depleted than for the disordered state of  $\text{Cu}_3\text{Au}$  [40]. This spatial compression on the 5d shells of Au is most likely due to the sp electrons compressing to a smaller atomic volume [35]. Therefore it is not surprising that in order to decrease this spatial compression on 5d electrons, the surface Au are displaced  $0.1 \text{ \AA}$  out of the surface. It remains to be seen whether similar changes in bonding and surface phonon dispersion occur on the disordered surface.

Force constant models that include noncentral forces will most likely change the interpretation of a stiffened force constant between the first- and second-layer Cu atoms. It has recently been shown through ab initio calculations how non-central forces influence the surface phonon spec-

trum [41]. For example, on a Al(001) surface the Rayleigh wave is higher in energy than what would be predicted by a central force constant model fit to the bulk phonon dispersions. It has been shown that this behavior is not due to a stiffening of the first- and second-layer force constants (which actually soften), but rather it is due to a more complicated many-body force [41,42]. Although calculations have only been performed on Al(001), Gasper and Eguiluz [42] believe that similar arguments should apply to Cu(001) as well. This tangential compressive stress has also been postulated by Heine and Marks for noble or nearly full d-shell metals [35]. Clearly, ab initio calculations would be useful to gain a better understanding of what changes in surface bonding occur.

## 8. Conclusion

In conclusion, we have presented phonon dispersion results along the  $\bar{\Gamma}-\bar{M}'$  direction for the ordered  $\text{Cu}_3\text{Au}(001)$  surface, where two surface modes are detected. Using a central potential force constant fitting procedure we have concluded that a 20% stiffening of the force constant between the first- and second-layer Cu atoms is needed to reconcile experiment and theory, and that slight relaxations of the first-layer nearest-neighbor tensions are necessary to match previous experimental data. Subsequent papers will deal with the higher-temperature surface structure and dynamics of this fascinating alloy, including an investigation of the surface phase transition. Ab initio calculations for both the ordered and disordered states would be most useful as we seek to understand the change in bonding which occurs as this phase transition is approached.

## Acknowledgements

We would like to thank T.M. Buck for providing the  $\text{Cu}_3\text{Au}$  sample and S. Katano for algebraic details concerning the bulk phonon analysis. Discussions and technical assistance provided by S.F. King are also gratefully acknowledged. This

work was supported, in part, by the Air Force Office of Scientific Research, the National Science Foundation Materials Research Laboratory at The University of Chicago, and the Research Corporation.

## References

- [1] For a recent review of some surfaces that have been studied, see: J.F. van der Veen and M.A. Van Hove, Eds., *The Structure of Surfaces II*, Vol. 11 of Springer Series in Surface Sciences (Springer, Berlin, 1988); Phonons 89, Eds. S. Hunklinger, W. Ludwig and G. Weiss (World Scientific, Singapore, 1990) p. 841; Proc. Tenth European Conference on Surface Science, Eds. C.M. Bertoni, F. Manghi and U. Valbusa, *Surf. Sci.* 211/212 (1989).
- [2] B. Gans, S.F. King, P.A. Knipp, D.D. Koleske and S.J. Sibener, *J. Electron Spectrosc. Relat. Phenom.* 54/55 (1990) 333; M. Wuttig, *J. Electron Spectrosc. Relat. Phenom.* 54/55 (1990) 383.
- [3] M. Mostoller, R.M. Nicklow, D.M. Zehner, S.-C. Lui, J.M. Mundenar and E.W. Plummer, *Phys. Rev. B* 40 (1989) 2856.
- [4] A.I. Taub and R.L. Fleisher, *Science* 243 (1989) 616; B.H. Kear, *Sci. Am.* 255 (1986) 159; R.L. Fleisher, D.M. Dimiduk and H.A. Lipsitt, *Annu. Rev. Mater. Sci.* 19 (1989) 231.
- [5] V.S. Sundaram, R.S. Alben and W.D. Robertson, *Surf. Sci.* 46 (1974) 653.
- [6] H.C. Potter and J.M. Blakely, *J. Vac. Sci. Technol.* 12 (1975) 635.
- [7] E.G. McRae and R.A. Malic, *Surf. Sci.* 148 (1984) 551.
- [8] T.M. Buck, G.H. Wheatley and L. Marchut, *Phys. Rev. Lett.* 51 (1983) 43.
- [9] G.W. Graham, *Surf. Sci.* 187 (1987) 490.
- [10] G.W. Graham, *Surf. Sci.* 137 (1984) L79.
- [11] K.D. Jamison, D.M. Lind, F.B. Dunning and G.K. Walters, *Surf. Sci.* 159 (1985) L451.
- [12] L. Guttman, in: *Solid State Physics*, Vol. 3, Eds. F. Seitz and D. Turnbull (Academic Press, New York, 1956).
- [13] (a) F.W. Jones and C. Stykes, *Proc. R. Soc. A.* 166 (1938) 376; (b) D.T. Keating and B.E. Warren, *J. Appl. Phys.* 22 (1951) 286.
- [14] (a) J.M. Cowley, *J. Appl. Phys.* 21 (1950) 24; (b) S.C. Moss, *J. Appl. Phys.* 35 (1964) 3574.
- [15] R. Lipowsky, *Ferroelectrics* 73 (1987) 69; *Phys. Rev. Lett.* 49 (1982) 1575.
- [16] S.F. Alvarado, M. Campagna, A. Fattah and W. Uelhoff, *Z. Phys. B (Condensed Matter)* 66 (1987) 103; H. Dosch and J. Peisl, *J. Phys. Paris Colloq. C* 7 (1989) 257;

- Surface Phonons, Vol. 21 of Springer Series in Surface Sciences, Eds. W. Kress and F.W. de Wette (Springer, New York, 1991).
- [17] S.F. King, D.D. Koleske, B. Gans and S.J. Sibener, to be published.
- [18] K. Kern and G. Comsa, in: *Advances in Chemical Physics*, Ed. K.P. Lawley (Wiley, Chichester, 1990) p. 211; J.P. Toennies, in: *Dynamics of Gas-Surface Interactions*, Eds. G. Benedek and U. Valbusa, Vol. 21 of Springer Series in Chemical Physics (Springer, Berlin, 1982).
- [19] J.H. Weare, *J. Chem. Phys.* 61 (1974) 2900.
- [20] Y.W. Yang, PhD Thesis, The University of Chicago, 1988; B. Gans, PhD Thesis, The University of Chicago, 1990; D.D. Koleske, Y.W. Yang, B. Gans, S.F. King, W.J. Menezes, S. Silence, H. Krebs and S.J. Sibener, to be published.
- [21] W.B. Pearson, *Handbook of Lattice Spacings and Structures of Metals* (Pergamon, Oxford, 1967).
- [22] G. Comsa, *Surf. Sci.* 81 (1979) 57.
- [23] W.A. Schlup and K.H. Rieder, *Phys. Rev. Lett.* 56 (1986) 73.
- [24] See, for example, eq. (5) of: P. Knipp and B.M. Hall, *Surf. Sci.* 224 (1989) L983.
- [25] A.C. Levi and H. Suhl, *Surf. Sci.* 88 (1979) 221.
- [26] V. Celli, G. Benedek, U. Harten, J.P. Toennies, R.B. Doak and V. Bortolani, *Surf. Sci.* 143 (1984) L376.
- [27] S. Katano, M. Iizumi and Y. Noda, *J. Phys. F (Met. Phys.)* 18 (1988) 2195.
- [28] T.E. Feuchtwang, *Phys. Rev.* 155 (1967) 715.
- [29] M. Wuttig, W. Hoffman, E. Preuss, R. Franchy, H. Ibach, Y. Chen, M.L. Xu and S.Y. Tong, *Phys. Rev. B* 42 (1990) 5443.
- [30] R.E. Allen, G.P. Alldredge and F.W. de Wette, *Phys. Rev. B* 4 (1971) 1661.
- [31] G.W. Farnell, in: *Acoustic Surface Waves*, Ed. A.A. Olinger (Springer, Berlin, 1978); R. Stonely, *Proc. R. Soc. (London) A* 232 (1955) 447.
- [32] Z.Q. Wang, Y.S. Li, C.K.C. Lok, J. Quinn, F. Jona and P.M. Marcus, *Solid State Commun.* 62 (1987) 181.
- [33] J.C. Hansen, M.K. Wagner and J.G. Tobin, *Solid State Commun.* 72 (1989) 319.
- [34] M. Wuttig, R. Franchy and H. Ibach, *Z. Phys. B (Condensed Matter)* 65 (1986) 71.
- [35] V. Heine and L.D. Marks, *Surf. Sci.* 165 (1986) 65.
- [36] M.S. Daw and M.I. Baskes, *Phys. Rev. B* 29 (1984) 6443.
- [37] A. Zangwill, in: *Physics at Surfaces* (Cambridge University Press, Cambridge, 1988) p. 29.
- [38] B. Ginatempo, G.Y. Guo, W.M. Temmerman, J.B. Staunton and P.J. Durham, *Phys. Rev. B* 42 (1990) 2761.
- [39] R.G. Jordan, *Vacuum* 38 (1988) 267.
- [40] T.K. Sham, Y.M. Yiu, M. Kuhn and K.H. Tan, *Phys. Rev. B* 41 (1990) 11881.
- [41] A.G. Eguiluz, *Phonon 89*, Eds. S. Hunklinger, W. Ludwig and G. Weiss (World Scientific, Singapore, 1990) p. 851.
- [42] J.A. Gasper and A.G. Eguiluz, *Phys. Rev. B* 40 (1989) 11976.